JGR Solid Earth

RESEARCH ARTICLE
10.1029/2018JB016837

Retrieval of Interstation Local Body Waves From Teleseismic Coda Correlations

E. Saygin[1,2] **and B. L. N. Kennett**[3]

[1]Deep Earth Imaging, Future Science Platform, CSIRO, Perth, Western Australia, Australia, [2]Department of Physics, School of Physics, Mathematics and Computing, University of Western Australia, Perth, Western Australia, Australia, [3]Research School of Earth Sciences, The Australian National University, Canberra, ACT, Australia

Key Points:
- We observe emergence of high-frequency interstation body wave reflections from the correlation of teleseismic coda arrivals across regional arrays
- The retrieved body waves at regional distances are useful to conduct local seismic imaging beneath seismic arrays
- Modeling with a simplified three-layer medium shows some level of agreement with the observed arrivals for Warramunga Array in Australia

Supporting Information:
- Supporting Information S1

Correspondence to:
E. Saygin,
erdinc.saygin@uwa.edu.au

Citation:
Saygin, E., & Kennett, B. L. N. (2019). Retrieval of interstation local body waves from teleseismic coda correlations. *Journal of Geophysical Research: Solid Earth*, *124*, 2957–2969. https://doi.org/10.1029/2018JB016837

Received 5 OCT 2018
Accepted 9 MAR 2019
Accepted article online 13 MAR 2019
Published online 25 MAR 2019

Abstract We retrieve the local *P* wave empirical Green's functions between the elements of five different regional arrays across the globe by cross-correlating and bin stacking the teleseismic earthquake coda waves recorded at each array. The stack is made using the coda of *P* and *S* wave phases for events in the distance range from 40° to 50° from the center of the array. With a sequence of time windows along the coda the various body wave arrivals can be tracked, using record sections constructed by binning the stacked interstation correlograms in less than 1-km distance increments. The correlation of the coda part of each principal seismic phase produces highly coherent interstation arrivals for different analysis windows. Such arrivals can be reproduced by just stacking 100 arrivals from a pool of more than a thousand events, showing the stability of the observed Green's functions. Modeling for the structure beneath the Warramunga array in the Northern Territory, Australia, demonstrates that these arrivals correspond to multiply reflected arrivals from layers at different depths. The recovery of high-frequency interstation body waves from the teleseismic earthquake coda opens the prospect of conducting local high-resolution seismic imaging with teleseismic energy.

1. Introduction

Despite a low signal-to-noise ratio, body waves have been successfully extracted from the autocorrelation and cross correlation of ambient seismic noise and earthquake coda. Roux et al. (2005) demonstrated the body wave component of Green's function from ambient noise cross correlations at the Parkfield seismic array. For the shallow Earth, Draganov et al. (2007) retrieved body wave reflections from an exploration scale array with a recording duration less than 24 hr. Nakata et al. (2015) used seismic noise recorded across a dense array in California to extract coherent diving body waves and imaged the subsurface structure with travel time tomography. More recently, Zhou and Paulssen (2017) analyzed borehole seismic noise data and extracted *P* and *S* waves from noise correlations. For larger scales, many other studies have retrieved and used body waves sampling the deeper subsurface from the cross correlation of seismic noise (Boué et al., 2013; Feng et al., 2017; Lin et al., 2013; Nishida, 2013; Poli et al., 2015).

As in the use of the ambient seismic noise wavefield, it is possible to use the correlation between different sensors in the coda field to extract an approximate version of the empirical Green's function between two points from multiply scattered seismic waves. Although the two applications are similar, the higher amplitudes in the seismic coda allow more facets of Green's function to emerge. However, the use of seismic coda to extract body and surface waves within a cross-correlation framework is still limited. Campillo and Paul (2003) were able to extract coherent information on surface waves over reasonably large distances in Mexico from the seismic coda of larger events. Tonegawa et al. (2009) used *S* wave coda recorded across Japan to retrieve the direct and reflected body waves at relatively low frequencies. Ruigrok et al. (2010) used distant earthquake reverberations to conduct imaging across a 2-D array in the United States. Lin and Tsai (2013) used antipodal station pairs to extract global body wave phases by cross-correlating noise and earthquake coda. Boué et al. (2014) retrieved deep seismic phases by correlating continuous broadband records containing seismic ambient noise and coda waves exploiting reverberation and scattering. Recently, Pham et al. (2018) correlated the later part of the coda wavefield of large earthquakes and found a good match between the observed correlograms and simulations including previously unobserved phases.

In addition to the coda and noise cross correlations, the autocorrelation of the seismic noise and teleseismic earthquake coda, and reverberations to extract reflectivity response beneath a seismic station, has

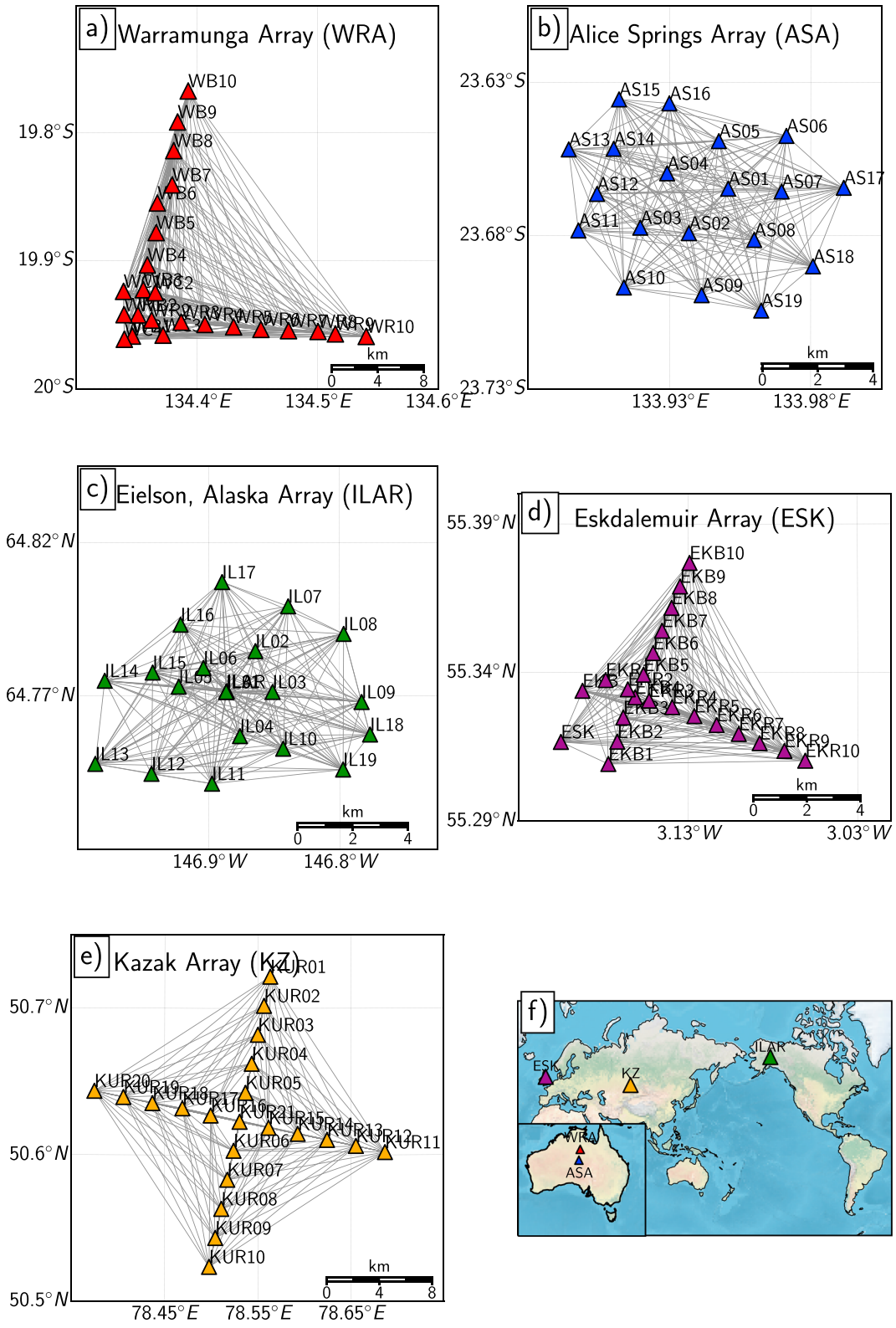

Figure 1. (a) The configuration of the Warramunga array (WRA) in Australia, showing the interstation paths. (b) The configuration of the Alice Springs array (ASA) in Australia, showing the interstation paths. (c) Eielson, Alaska Array (ILAR), USA. (d) Eskdalemuir Array (ESK) in Scotland. (e) Kazak Array (KZ) in Kazakhstan. (f) The inset map shows the distribution of arrays.

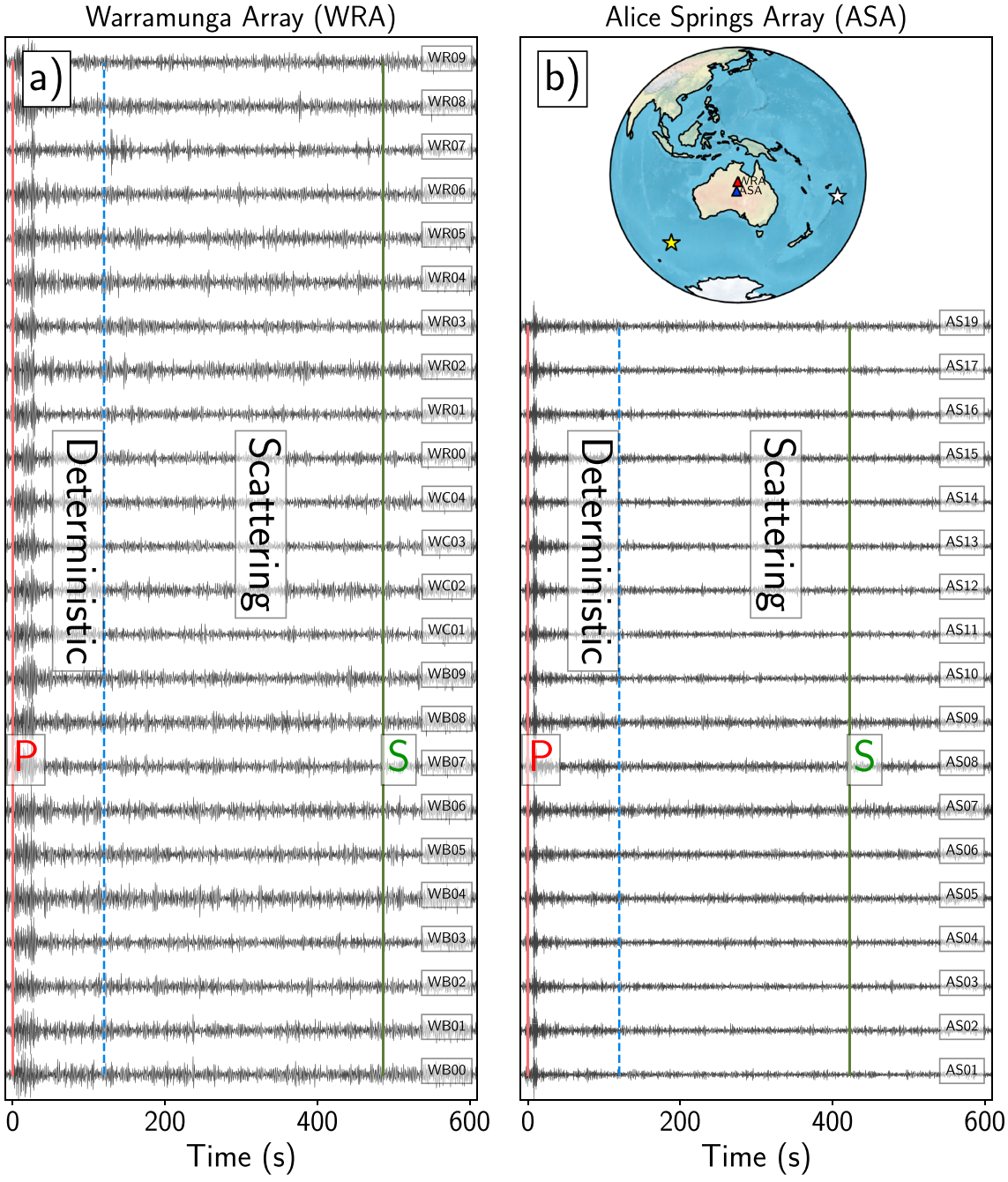

Figure 2. (a) Coda waves following the main *P* and *S* wave arrivals from an event in South East Indian Ridge with magnitude $M_w = 5.4$ and a depth of 10 km at the Warramunga array. (b) Coda waves following the main *P* and *S* wave arrivals from an event in Tonga Arc with magnitude $M_w = 5.0$ and a depth of 10 km at the Alice Springs array. In both panels, the later coda becomes more chaotic as multiply scattered waves dominate especially after 130 s (blue dash line). The traces have been band-pass filtered from 1 to 5 Hz and normalized to unity. The inset map shows the location of events with yellow and white stars (South East Indian Ridge and Tonga Islands).

been demonstrated across Australia, Europe, Indonesia, Turkey, and the whole Earth by multiple studies of Becker and Knapmeyer Endrun (2017), Gorbatov et al. (2012), Kennett (2015), Pham and Tkalčić (2017), Poli et al. (2017), Ruigrok and Wapenaar (2012), Saygin et al. (2017), Sun and Kennett (2016), Sun et al. (2018), and Taylor et al. (2016). In all of these studies, the body wave reflectivity response of the Earth beneath a seismic station is extracted and used in inferring the underlying structure.

In this study, we use multiple regional arrays around the globe with tight station spacing, mostly located in regions with low anthropogenic noise levels. For example, the Warramunga seismic array in Australia has

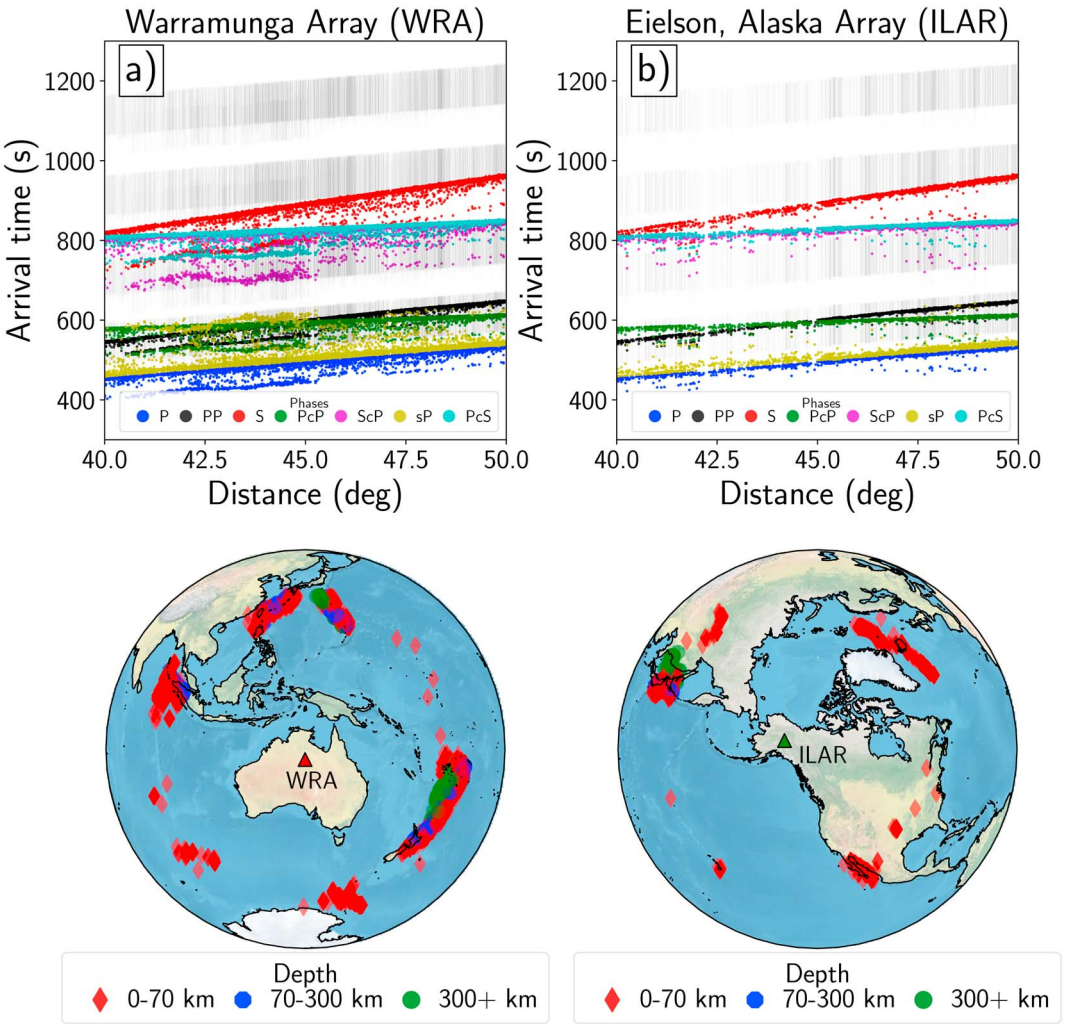

Figure 3. Selected time windows as a function of phase for the Warramunga (WRA) and Eielson (ILAR) arrays.

the ability to record both regional and teleseismic earthquakes with well-developed coda waves. Previous work by Kennett and Furumura (2008) showed that the highly energetic coda waves from Indonesian events observed across Australian stations arise from strong internal scattering within the thick cratonic continental Australian lithosphere, helped by high Q as well as the geometry of the subducting slab. Later work by Kennett and Furumura (2013) and Kennett et al. (2014) described P_o and S_o phases (oceanic P_n and S_n) propagating over old and thick oceanic lithosphere for large distances. These phases and their coda waves crossing old oceanic lithosphere were observed well beyond 30° between 1 and 5 Hz. Kennett and Furumura (2016) studied the effect of multiscale heterogeneity on the propagation of seismic waves across Australian continent both with observations and numerical simulations to confirm the role of the efficient internal scattering by lithospheric heterogeneities for generating the prolonged coda waves observed at seismic stations across Australia.

For all of the seismic arrays, we use the well-developed high-frequency coda waves from teleseismic earthquakes. The interaction of seismic waves with oceanic and continental structure yields a long duration of complex seismic coda, and the local scattering helps with the extraction of interstation body and surface waves sampling the subsurface structure beneath the array. We employ the stacked cross correlations of the coda of P and S waves, between all of the elements of the array, for seismic events in a limited distance range from the array to extract local interstation P wave empirical Green's functions. The incoherent scattered wavefield generated from the incident waves by the inhomogeneities in the medium has sufficient amplitude that the body wave components of the local Green's function can be raised above the intrinsic noise level.

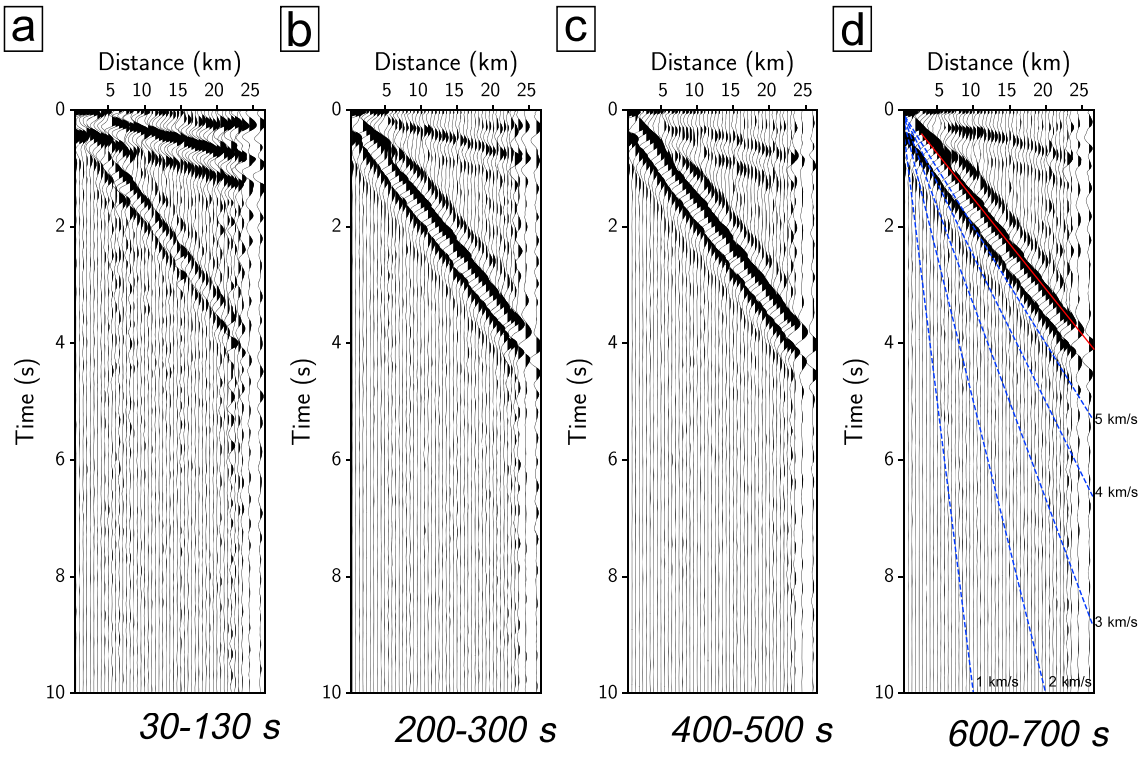

Figure 4. Coda correlograms showing the evolution of the interstation *P* wave Green's functions for Warramunga Array for analysis windows of 30–130, 200–300, 400–500, and 600–700 s after *P*. Waveforms are filtered between 1 and 5 Hz and normalized to unity. The red line shows the approximate location of the maximum amplitude of the body wave arrivals.

2. Data

We use multiple regional seismic arrays with different configurations around the globe, as shown in Figure 1f. Each array has short period and/or broadband seismic sensors with vertical or three-component recordings. We only use the vertical components in our analyses to retrieve the *P* wave component of the interstation propagation. We briefly describe the configuration of each array: The Warramunga Array (WRA) in the Northern Territory of Australia, near the town of Tennant Creek, has operated since 1968 and was upgraded in 1999 to meet the requirements of a primary seismic station for the Comprehensive Nuclear-Test-Ban Treaty. WRA now comprises 24 elements, all with broadband vertical seismometers. The array shape is given in Figure 1a. The data are digitized at each sensor at 40 Hz. The array pattern provides a broad range of interstation separations ranging from 0.8 km to about 26 km. WRA sits more than 500 km from the coastline in the interior of Australia so that the ambient noise level is relatively low. We use data recorded between 2000 and 2017 across the array. During this period, some of the elements of the array were offline for some time.

The Alice Springs Array is also located in the Northern Territory of Australia with 18 elements with short period sensors and a single broadband sensor with a sampling rate of 20 Hz. The station spacing ranges from 2 km to over 10 km (Figure 1b). As in WRA case, the ambient noise levels are relatively low given its distance from the coastline, which is over 700 km. In the analyses, we use data from 2003 to 2017.

The Eielson Array (ILAR) is in Alaska, USA. The array has 21 elements with the short period and broadband sensors (Figure 1c). ILAR-like WRA is part of Comprehensive Nuclear-Test-Ban Treaty primary monitoring network. We use teleseismic earthquakes recorded across the array from 2003 to 2017.

The Eskdalemuir Array (ESK) is in Scotland, United Kingdom. The array has an L-shaped orientation with 20 elements equipped with mostly broadband sensors (Figure 1d) similar to WRA. We use event data recorded between 2014 and 2017.

The last seismic array is from Kazakhstan. The data archive contains events from 1995 to 2017, with different levels of data coverage. The configuration of the array is cross shaped with 21 elements, as shown in

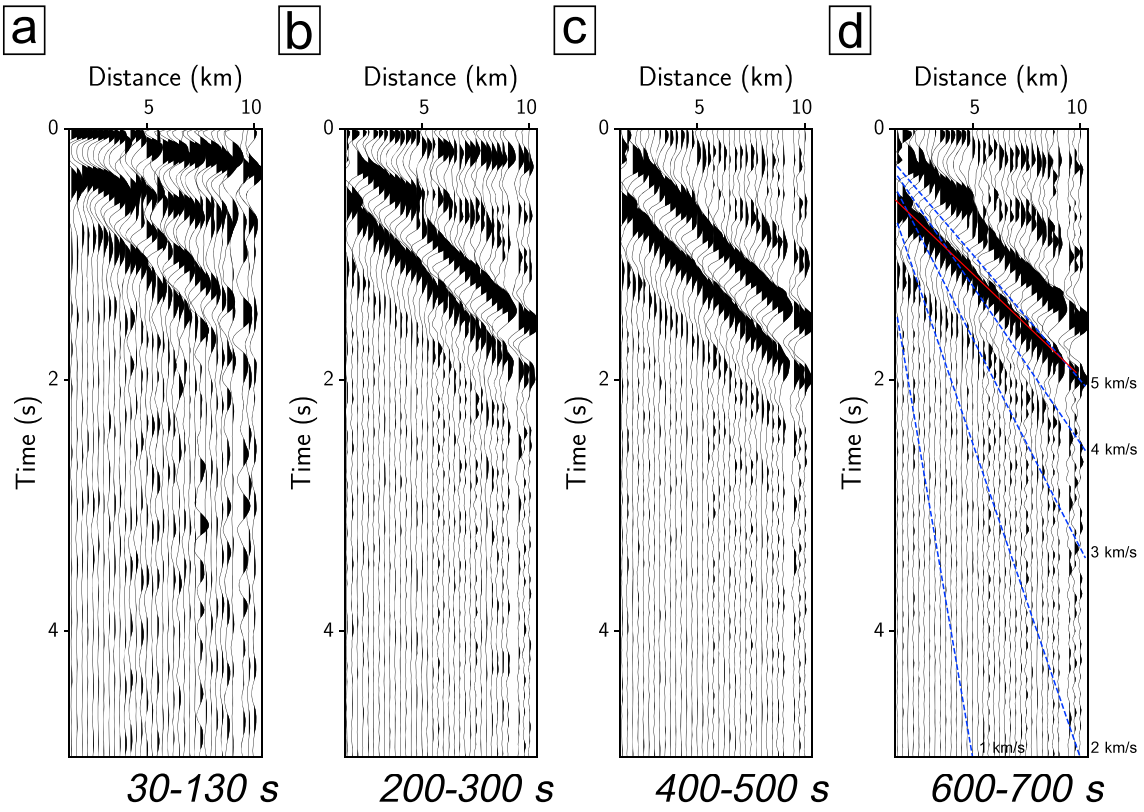

Figure 5. Coda correlograms showing the evolution of the interstation *P* wave Green's functions for ASA for analysis windows of 30–130, 200–300, 400–500, and 600–700 s after *P*. Waveforms are filtered between 1 and 5 Hz and normalized to unity. The red line shows the approximate location of the maximum amplitude of the body wave arrivals.

Figure 1e. The sensor technology of the array was upgraded during the operation period. We use recordings from both broadband and short period sensors.

In addition to these arrays, we have tested coda correlation for other regional arrays. We find that the local ambient seismic noise levels play a substantial role in the recovery rate. For instance, Yellow Knife Array in Canada shows a seasonal variation in the recovery rate and the signal-to-noise ratio (SNR) of the body and surface waves, where the seasonal variability of the ambient seismic noise wavefield was previously reported by Koper et al. (2009) and Xu et al. (2017). We show results for Yellow Knife Array in the supporting information.

3. The Nature of the Near-Teleseismic Coda

In this work we employ the coda of teleseismic events in the epicentral distance range 40–50° from the various arrays. The early part of the wavetrain, immediately following *P*, is dominated by local reverberations and conversions that can be exploited in receiver function or autocorrelation studies. After about 120 s the scattering in the lithosphere beneath and around the stations becomes dominant. It is this locally scattered component of the wavefield that is exploited by our cross correlations. We illustrate the nature of the coda at the Warramunga and Alice Springs arrays for two modest size events in the South East Indian Ridge and Tonga Arc in Figure 2, showing the frequency band from 1 to 5 Hz. We see considerable coherence in the nature of the wavefield across both arrays for the first minute after the *P* arrival. This coherency diminishes with increasing time, and by 130 s we have reached the point where we have a well-developed scattered field whose properties reflect the local conditions. Ahead of the *S* phase, the vertical component records are dominated by *P* to *P* scattering.

The scattered field extends well beyond the onset of *S*. Efficient scattering from *S* to *P* is also picked up on the vertical component seismometers. This means that there is a substantial interval of time for which it is possible to extract information about *P* waves from the cross correlation of the stations in the array. In later

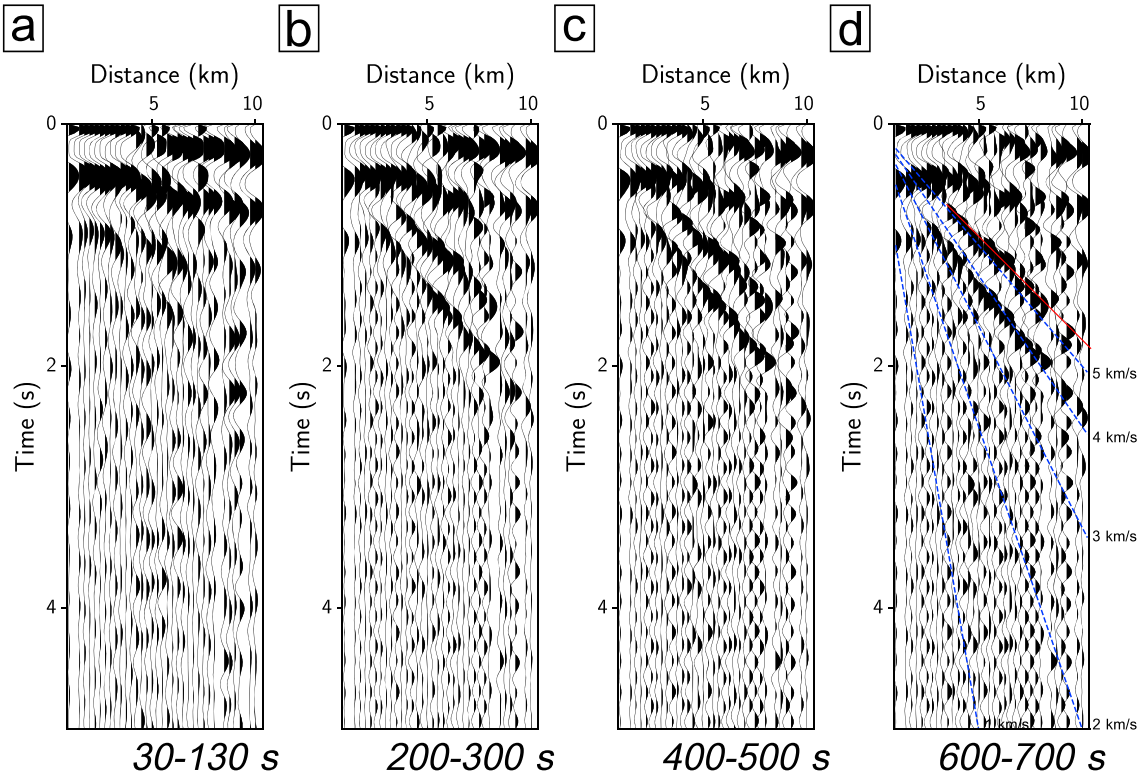

Figure 6. Coda correlograms showing the evolution of the interstation *P* wave Green's functions for Eielson Array for analysis windows of 30–130, 200–300, 400–500, and 600–700 s after *P*. Waveforms are filtered between 1 and 5 Hz and normalized to unity. The red line shows the approximate location of the maximum amplitude of the body wave arrivals.

sections, we display the results from successive windows in the coda so the evolution of the signal of local structure can be followed.

4. Method

A set of 100-s coda time windows for the intervals 30–130, 200–300, 400–500, and 600–700 s after the onset of *P* from each event is used to construct the cross correlations between the elements of the array. The suite of fixed length windows with variable time offset enables us to follow the evolution of the correlated phases along the coda. The expected times for the *P* arrivals are calculated using the *ak135* velocity model (Kennett et al., 1995). The correlograms for each coda segment are then stacked to enhance the signal-to-noise ratio. After normalizing the record sections, the cross correlograms are computed from the records of the stations from each array for each of the selected time windows. To improve the clarity of the record section, we have organized the cross correlograms in distance bins smaller than 1 km and stacked all the available correlograms in each bin. This operation averages out any lateral heterogeneities and retrieves the response of an average 1-D structure beneath the array. A final sum is made over causal and acausal parts of each signal. As the last step, we apply a band-pass filter between 1 and 5 Hz to improve the signal-to-noise ratio of the body and surface waves in each cross-correlogram display.

We define our bin stacking procedure as

$$\hat{C}_{\text{bin}}(t, d_j) = \frac{1}{N_i M_j} \sum_{i=1}^{N_i} \sum_{k=1}^{M_j} C_{ab}(t, n_i, d_k), \tag{1}$$

where C_{ab} is the cross correlogram between stations a and b, t is the selected coda window used in the cross correlations, d_k the interstation distance, d_j is the distance bin of interest, and N_i and M_j are the total number of station pairs used in stacking and the total number of event couples for which $d_j - \Delta d/2 \leq d_k < d_j + \Delta d/2$, where Δd is the bin width.

The distribution of the events recorded at the WRA and ILAR arrays used in this study is shown in Figure 3. All events are in the teleseismic range. The incident plane waves (*P* wave) for each of the events

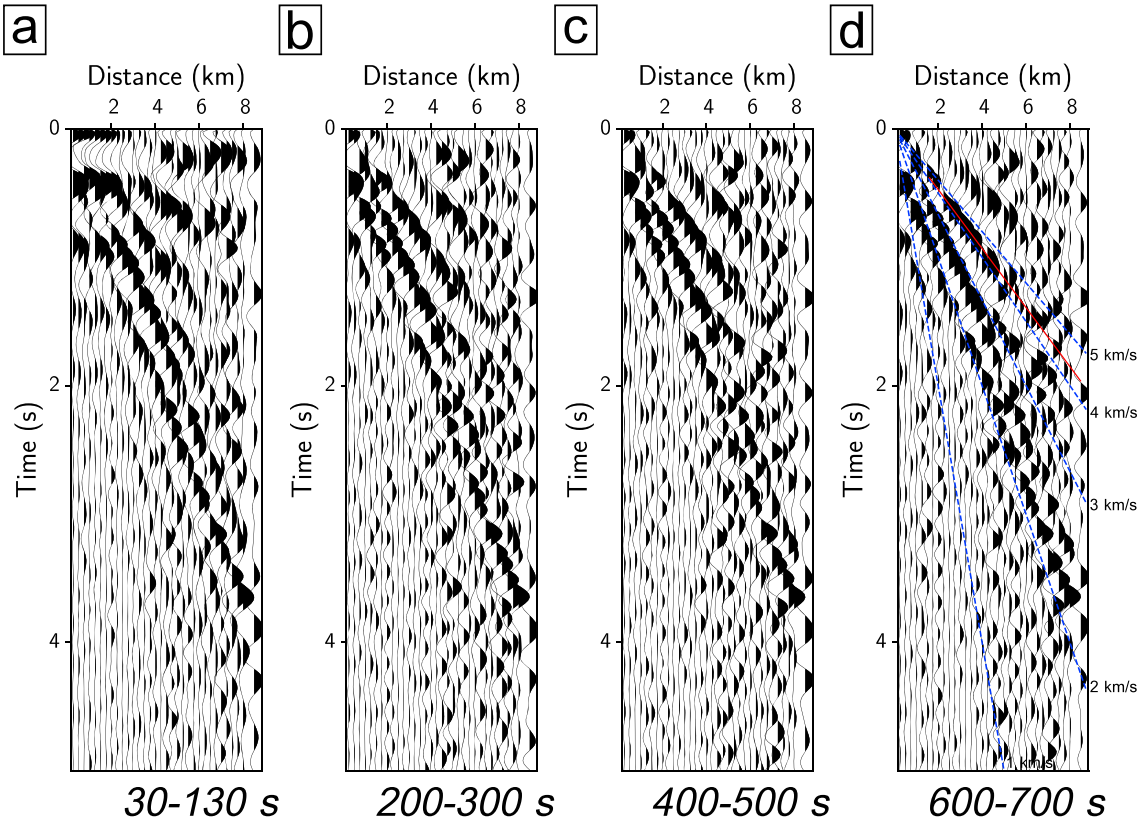

Figure 7. Coda correlograms showing the evolution of the interstation *P* wave Green's functions for Eskdalemuir Array for analysis windows of 30–130, 200–300, 400–500, and 600–700 s after *P*. Waveforms are filtered between 1 and 5 Hz and normalized to unity. The red line shows the approximate location of the maximum amplitude of the body wave arrivals.

across the 26-km aperture arrays can be characterized by a plane wave with a slowness around 6.2 s/deg (apparent velocity ≈18 km/s). The data for each event were band-pass filtered from 1 to 5 Hz to emphasize the contribution of the scattered wavefield in the cross-correlation computations.

5. Local Body Waves

In Figure 3, the arrival time of a number of different seismic phases for each event is given along with scaled correlation windows for the Warramunga and ILAR. In these analysis windows, we effectively cross-correlate the *P* wave coda for the first two windows [30–130 and 200–300 s] and the *S* wave coda for the last two windows [400–500 and 600–700 s]. However, the vertical component records are expected to be dominated by *P* wave contributions rather than *S*. We display the results of the cross correlation and stacking for the different arrays in Figures 4–8. The early part of the cross-correlation sections corresponds to the direct and refracted part of the wavefield, which is visible as planar arrivals with varying apparent velocities for the different arrays. In the next window [200–300 s], the amplitudes of these planar arrivals diminish. The third panel [400–500 s] shows teleseismic planar arrivals some with the *S*-type arrivals. The last panel indicates some arrivals with similar apparent velocities to the first two windows.

5.1. Warramunga

We use over 5,000 teleseismic events recorded between 2000 and 2017 with magnitudes from 5.5 to 7.0. Each correlogram was bin stacked with a 0.5-km bin width. In the later part of each section displayed in Figure 4, a coherent type of arrival can be observed with very clear moveout and also some later arrivals with weaker amplitudes starting from 4 s. The first branch of these arrivals begins to develop at around 1 s and is then visible to the largest moveout bin at 26 km. The typical interval velocity of these arrivals is calculated as ≈ 6.0 km/s, which is close to the local *P* wave velocities. For the correlation window 400–500 s, despite the fact that the incoming teleseismic wavefield is planar *S* waves, Green's functions continue to show *P* wave-type arrivals with the same moveout. Similar observations were made by Tonegawa et al. (2009)

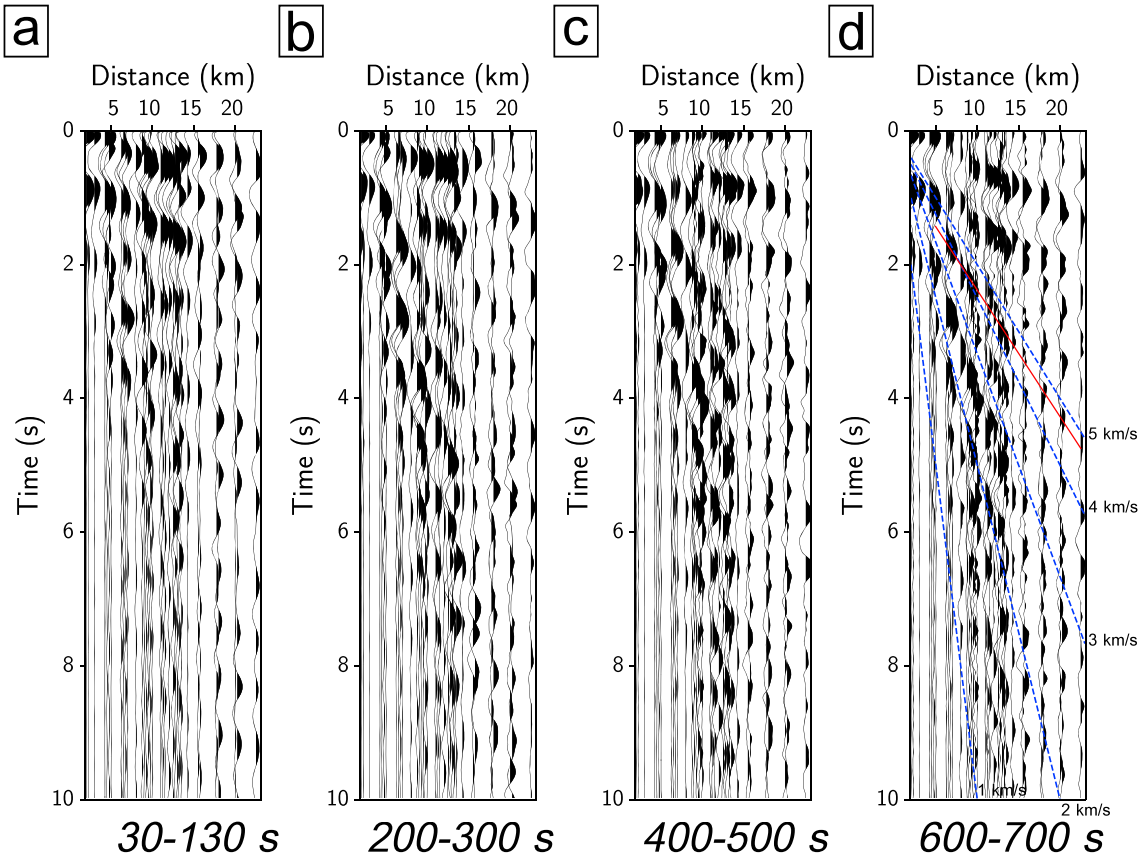

Figure 8. Coda correlograms showing the evolution of the interstation *P* wave Green's functions for Kazak Array for analysis windows of 30–130, 200–300 , 400–500, and 600–700 s after *P*. Waveforms are filtered between 1 and 5 Hz and normalized to unity. The red line shows the approximate location of the maximum amplitude of the body wave arrivals.

for teleseismic *S* wave coda correlations, where clear interstation *P* waves are observed. Local scatterers in the layered medium contribute to efficient scattering and therefore *S*-*P* phase conversion and also rapid attenuation of *S* waves. The *P* waves are enhanced because we consider the cross correlation of vertical component records.

5.2. ASA

We use over 4,300 teleseismic events recorded between 2003 and 2017 with magnitudes from 5.5 to 7.5. Each correlogram was stacked using a 0.25-km bin width. The stacked correlations show clear arrivals with a velocity of around ≈ 5.0 km/s across all of the sections (Figure 5) similar to WRA.

5.3. ILAR

We use over 1,780 events recorded between 2003 and 2007 with magnitudes from 5.5 to 7.0. The bin stacking was conducted with 0.25-km bin width. The coda correlations for the ILAR array show clearly developed body-type arrivals with a velocity of around 5.5 km/s (Figure 6). These arrivals can be tracked from the interstation distance of 1 km to the largest bin distance of 10.25 km. As in the previous case, the first analysis window of 30–130 is dominated by planar arrivals, whereas in the later windows local body wave propagation becomes much more dominant.

5.4. ESK

The available data from the ESK array only start from 2014. We extract 599 events recorded between 2014 and 2017 with magnitudes from 5.5 to 7.0. Bin stacking was conducted with a 0.25-km bin width. The coda correlation of the arrivals shows high signal-to-noise ratio surface waves with group velocities around 2.5 km/s dominating most of the records (Figure 7). However, in addition to the surface waves and teleseismic planar arrivals, a second branch of arrivals with relatively high velocities of 4.4-5 km/s can be tracked across the whole section indicating the presence of body-type propagation between stations. Because we do not

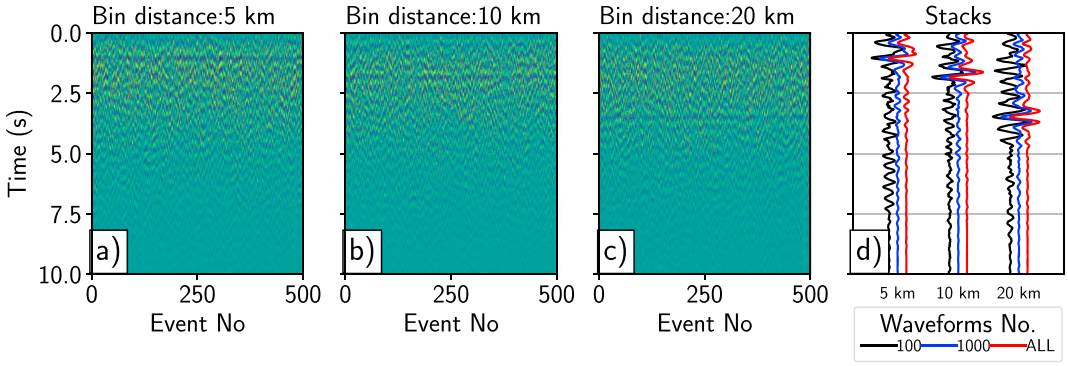

Figure 9. (a) Section plot of randomly selected 500 events used in coda correlations for bin distance 5 km at Warramunga Array. (b) 10 km. (c) 20 km. (d) The evolution of the signal-to-noise ratio of stacked waveforms for different bins with randomly selected 100 and 1,000 events and also for all of the events. Waveforms are filtered between 1 and 5 Hz and normalized to unity.

use active suppression of surface waves to avoid processing bias, there is potential to boost the body wave arrivals by actively targeting the surface waves.

5.5. KZ

We use over 3,000 events recorded between 1995 and 2017 with magnitudes from 5.5 to 7.5. The bin stacking was conducted with 0.25-km bin width. The Kazak array is a cross-shaped array, as a result there are large gaps in the regular bins at longer distances. This means it is slightly more difficult to track energy across the seismic section than for the other arrays. However, in addition to surface waves and teleseismic body waves, a clear package of energy can be tracked across all of the sections with a velocity of 4.4 km/s, whereas surface waves arrive with a velocity of 2.9 km/s (Figure 8).

5.6. Stability of Observed Phases

We study the stability of the correlation procedure by using the results from the Warramunga and ASAR arrays. The stability and the coherency of each suite of coda correlation are investigated by using a randomly selected group of 500 events from over 5,000 available recordings. Linear stacking is then conducted for bin distances of 5, 10, and 20 km (Figure 9) for the WRA and 3, 5, and 10 km for the Alice Spring Array. For all of the event sections, a clear body arrival is visible with a very little moveout. The stacked waveforms have a high signal-to-noise ratio, with identical arrival times as shown in Figures 9 and 10. This demonstrates the potential of the technique, where even a small number of recorded events can produce coherent interstation body wave propagation, which can be useful for local body wave imaging.

5.7. Modeling of Arrivals-WRA

In the neighborhood of the WRA there is existing structural information available from refraction studies (Finlayson, 1981, 1982) and a recent 2-D seismic reflection line. We have built a simple 1-D model from

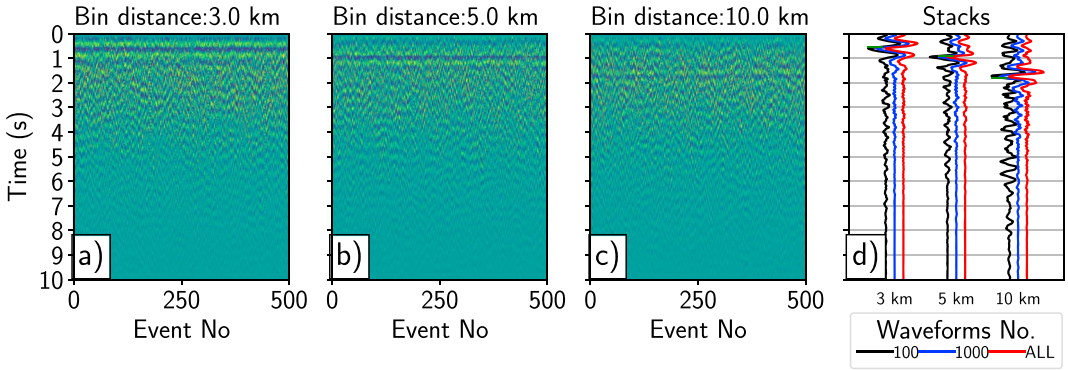

Figure 10. (a) Section plot of randomly selected 500 events used in coda correlations for bin distance 5 km at Alice Springs Array. (b) 10 km. (c) 20 km. (d) The evolution of the signal-to-noise ratio of stacked waveforms for different bins with randomly selected 100 and 1,000 events and also for all of the events. Waveforms are filtered between 1 and 5 Hz and normalized to unity.

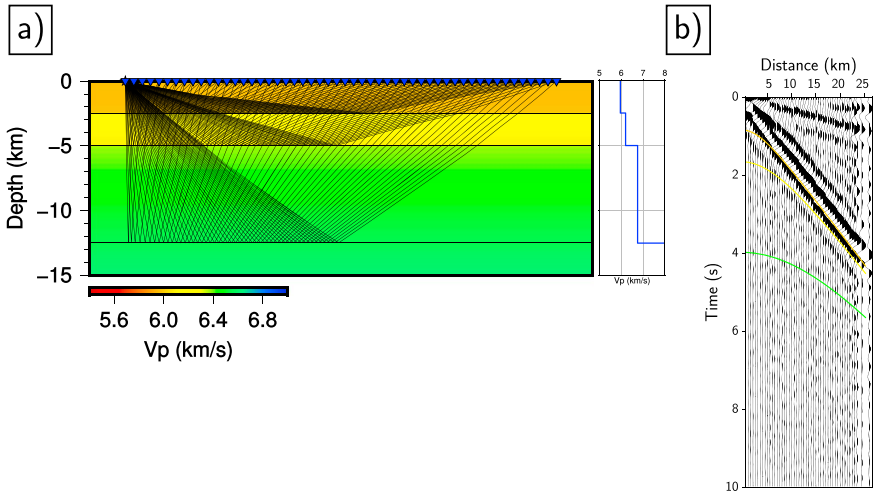

Figure 11. (a) Layered model used in travel time calculations. (b) Reflection section with travel times for Warramunga Array. Color coding corresponds to the layers in the model.

this information, but this undoubtedly presents an oversimplified picture of the structure in this hard rock domain. On the NS reflection line which lies about 25 km to the east of the array, there is considerable variability in the reflection response along the profile. All reflectors are weak and may well represent variations in the texture of the rocks rather than significant velocity contrasts. Velocity analysis proved to be difficult because moveout was hard to track.

With these limitations in mind, we have conducted ray-based modeling for the simplified structure using the Fast Marching Method of Rawlinson and Sambridge (2004), with a receiver geometry identical to our 1-D binned stacked waveforms. In Figure 11a, the model geometry is displayed along with the reflected rays. The ray analysis shows that the first two arrivals are hard to discriminate, because of the small separation in time between the reflections from the base of the first two layers. The reflections tend to merge to give travel times corresponding to the main observed branch. The reflection from the last layer at a depth of 12.5 km shows arrivals with some level of agreement with a very weak branch visible in Figure 11b at around 4 s. We use the 30- to 130-s window of the coda for these comparisons, where *P* coda will carry the most energetic part of the arrivals.

6. Discussion and Conclusions

The configuration of the long established seismic arrays and plentiful seismicity in a similar distance range has enabled us to capture the local *P* component of the local empirical Green's function from the correlation of waveforms of the *P* and *S* wave coda at relatively high frequencies, with different maximum interstation separations ranging from 8.5 to 26.5 km.

In general, it is harder to extract body waves from correlation studies than surface waves. This is the first time local high-frequency body waves have been extracted from the coda waves of distant earthquakes at different arrays. Previous studies reported the observation of higher mode Rayleigh waves especially across sedimentary basins, for example, Boué et al. (2016), Savage et al. (2013), and Saygin et al. (2016). In general higher mode Rayleigh waves arrive earlier than the fundamental modes. This has been documented in other studies such as Wang et al. (2017). For a similar aperture, large-N array, Wang et al. (2017) found the average Rayleigh wave phase velocities at around 3.98 km/s for 1.5 s and 4.42 km/s for 2.5 s across Mount St. Helens. We conduct a dispersion calculation for Rayleigh wave phase and group velocities of fundamental and first higher mode using the same velocity model in Figure 5 for WRA (in supporting information). The results show the highest phase velocity for the first higher mode around 5 km/s for 0.1 Hz. However, these velocities rapidly decline with the increasing frequencies especially at our measurement range of 1–5 Hz. We also observe a relative increase in the body wave velocities at far offsets especially for WRA, Alice Springs Array, and ILAR arrays (Figures 4–8), where surface wave-type arrivals normally follow a linear pattern.

To enhance the signal from the local structure, we can combine the results from the stacked cross correlations over multiple events in the different time windows to provide further signal enhancement particularly for refracted arrivals. Extra information on the reflected field can be extracted from the autocorrelation of the immediate coda of *P* (Sun & Kennett, 2016) using the same set of events.

Sens-Schönfelder et al. (2015) conducted a thorough analysis of the equipartitioning properties of the coda waves by studying the deep Okhotsk event from 2013. They concluded that the earlier part of the coda of a teleseismic event (<5,000 s) is suitable for local body wave retrieval with mainly isotropic propagation. In contrary, coda waves at longer periods and at later lag times are less sensitive to the local crust and therefore not equipartitioned. We keep our analysis windows restricted to less than 700 s after the arrival of teleseismic *P* waves. The consistency of the retrieved local body waves for each time window shows the coherency of the extraction process.

Thus, with care, it is possible to use passive recordings of distant earthquakes to generate record sections for both the body wave and surface wave components of the wavefield across a dense network. The cross correlograms allow the construction of reflection sections that constrain the near-surface wavespeeds quite well. The use of seismic coda from larger teleseismic events can thus provide a means of characterizing the seismic properties of a locality with purely passive recording, provided that broadband high-fidelity recordings of ground motion are available. The good results obtained for stations separated by more than 5 km at different arrays indicate that the individual stations in a network do not need to be closely spaced (<1 km) for relevant information to be extracted. All the arrays we have used are on hard rock sites, but the approach will work equally well for networks of stations across sedimentary structures. Indeed, the presence of sediments with stronger contrasts in physical properties will be advantageous for the extraction of reflections.

Acknowledgments
The authors wish to thank the Editor and two anonymous reviewers for their constructive suggestions. We thank RSES technical staff for their assistance in handling the waveform data. Figures are drafted with Python module-Matplotlib (Hunter, 2007). FM3D (de Kool et al., 2006) software package is used in the travel time modeling of the reflected phases. The facilities of IRIS Data Services, and specifically the IRIS Data Management Center, were used for access to waveforms, related metadata, and/or derived products used in this study. IRIS Data Services are funded through the Seismological Facilities for the Advancement of Geoscience and EarthScope (SAGE) Proposal of the National Science Foundation under Cooperative Agreement EAR-1261681. Most of the array data are available from IRISDMC database (http://ds.iris.edu/ds/nodes/dmc/). The Warramunga data set between 2000 and 2004 is archived at the Research School of Earth Sciences, ANU. Data access may be arranged by request to ansir@anu.edu.au.

References

Becker, G., & Knapmeyer Endrun, B. (2017). Crustal thickness across the Trans-European Suture Zone from ambient noise autocorrelations. *Geophysical Journal International*, *212*(2), 1237–1254.

Boué, P., Denolle, M., Hirata, N., Nakagawa, S., & Beroza, G. C. (2016). Beyond basin resonance: Characterizing wave propagation using a dense array and the ambient seismic field. *Geophysical Journal International*, *206*(2), 1261–1272.

Boué, P., Poli, P., Campillo, M., Pedersen, H., Briand, X., & Roux, P. (2013). Teleseismic correlations of ambient seismic noise for deep global imaging of the Earth. *Geophysical Journal International*, *194*(2), 844–848.

Boué, P., Poli, P., Campillo, M., & Roux, P. (2014). Reverberations, coda waves and ambient noise: Correlations at the global scale and retrieval of the deep phases. *Earth and Planetary Science Letters*, *391*, 137–145.

Campillo, M., & Paul, A. (2003). Long-range correlations in the diffuse seismic coda. *Science*, *299*(5606), 547–549.

de Kool, M., Rawlinson, N., & Sambridge, M. (2006). A practical grid-based method for tracking multiple refraction and reflection phases in three-dimensional heterogeneous media. *Geophysical Journal International*, *167*(1), 253–270.

Draganov, D., Wapenaar, K., Mulder, W., Singer, J., & Verdel, A. (2007). Retrieval of reflections from seismic background-noise measurements. *Geophysical Research Letters*, *34*, L04305. https://doi.org/10.1029/2006GL028735

Feng, J., Yao, H., Poli, P., Fang, L., Wu, Y., & Zhang, P. (2017). Depth variations of 410 km and 660 km discontinuities in eastern North China Craton revealed by ambient noise interferometry. *Geophysical Research Letters*, *44*, 8328–8335. https://doi.org/10.1002/2017GL074263

Finlayson, D. (1981). Reconnaissance of upper crustal seismic velocities in the tennant creek block, northern territory. *BMR Journal of Australian Geology and Geophysics*, *6*, 245–252.

Finlayson, D. (1982). Seismic crustal structure of the proterozoic North Australian Craton between Tennant Creek and Mount Isa. *Journal of Geophysical Research*, *87*(B13), 10,569–10,578.

Gorbatov, A., Saygin, E., & Kennett, B. (2012). Crustal properties from seismic station autocorrelograms. *Geophysical Journal International*, *192*(2), 861–870.

Hunter, J. D. (2007). Matplotlib: A 2D graphics environment. *Computing in Science & Engineering*, *9*(3), 90–95.

Kennett, B. (2015). Lithosphere-asthenosphere P-wave reflectivity across Australia. *Earth and Planetary Science Letters*, *431*, 225–235.

Kennett, B., Engdahl, E., & Buland, R. (1995). Constraints on seismic velocities in the Earth from traveltimes. *Geophysical Journal International*, *122*(1), 108–124.

Kennett, B., & Furumura, T. (2008). Stochastic waveguide in the lithosphere: Indonesian subduction zone to Australian craton. *Geophysical Journal International*, *172*(1), 363–382.

Kennett, B., & Furumura, T. (2013). High-frequency Po/So guided waves in the oceanic lithosphere: I—Long-distance propagation. *Geophysical Journal International*, *195*(3), 1862–1877.

Kennett, B., & Furumura, T. (2016). Multiscale seismic heterogeneity in the continental lithosphere. *Geochemistry, Geophysics, Geosystems*, *17*, 791–809. https://doi.org/10.1002/2015GC006200

Kennett, B., Furumura, T., & Zhao, Y. (2014). High-frequency Po/So guided waves in the oceanic lithosphere: II—Heterogeneity and attenuation. *Geophysical Journal International*, *199*(1), 614–630.

Koper, K. D., De Foy, B., & Benz, H. (2009). Composition and variation of noise recorded at the Yellowknife seismic array, 1991–2007. *Journal of Geophysical Research*, *114*, B10310. https://doi.org/10.1029/2009JB006307

Lin, F.-C., & Tsai, V. C. (2013). Seismic interferometry with antipodal station pairs. *Geophysical Research Letters*, *40*, 4609–4613. https://doi.org/10.1002/grl.50907

Lin, F.-C., Tsai, V. C., Schmandt, B., Duputel, Z., & Zhan, Z. (2013). Extracting seismic core phases with array interferometry. *Geophysical Research Letters*, *40*, 1049–1053. https://doi.org/10.1002/grl.50237

Nakata, N., Chang, J. P., Lawrence, J. F., & Boué, P. (2015). Body wave extraction and tomography at Long Beach, California, with ambient-noise interferometry. *Journal of Geophysical Research: Solid Earth*, *120*, 1159–1173. https://doi.org/10.1002/2015JB011870

Nishida, K. (2013). Global propagation of body waves revealed by cross-correlation analysis of seismic hum. *Geophysical Research Letters*, *40*, 1691–1696. https://doi.org/10.1002/grl.50269

Pham, T.-S., & Tkalčić, H. (2017). On the feasibility and use of teleseismic P wave coda autocorrelation for mapping shallow seismic discontinuities. *Journal of Geophysical Research: Solid Earth*, *122*, 3776–3791. https://doi.org/10.1002/2017JB13975

Pham, T.-S., Tkalčić, H., Sambridge, M., & Kennett, B. (2018). Earth's correlation wavefield: Late coda correlation. *Geophysical Research Letters*, *45*, 3035–3042. https://doi.org/10.1002/2018GL077244

Poli, P., Campillo, M., & de Hoop, M. (2017). Analysis of intermediate period correlations of coda from deep earthquakes. *Earth and Planetary Science Letters*, *477*, 147–155.

Poli, P., Thomas, C., Campillo, M., & Pedersen, H. A. (2015). Imaging the D" reflector with noise correlations. *Geophysical Research Letters*, *42*, 60–65. https://doi.org/10.1002/2014GL062198

Rawlinson, N., & Sambridge, M. (2004). Wave front evolution in strongly heterogeneous layered media using the fast marching method. *Geophysical Journal International*, *156*(3), 631–647.

Roux, P., Sabra, K. G., Gerstoft, P., Kuperman, W., & Fehler, M. C. (2005). P-waves from cross-correlation of seismic noise. *Geophysical Research Letters*, *32*, L19303. https://doi.org/10.1029/2005GL023803

Ruigrok, E., Campman, X., Draganov, D., & Wapenaar, K. (2010). High-resolution lithospheric imaging with seismic interferometry. *Geophysical Journal International*, *183*(1), 339–357.

Ruigrok, E., & Wapenaar, K. (2012). Global-phase seismic interferometry unveils P-wave reflectivity below the Himalayas and Tibet. *Geophysical Research Letters*, *39*, L11303. https://doi.org/10.1029/2012GL051672

Savage, M. K., Lin, F.-C., & Townend, J. (2013). Ambient noise cross-correlation observations of fundamental and higher-mode Rayleigh wave propagation governed by basement resonance. *Geophysical Research Letters*, *40*, 3556–3561. https://doi.org/10.1002/grl.50678

Saygin, E., Cummins, P., Cipta, A., Hawkins, R., Pandhu, R., Murjaya, J., et al. (2016). Imaging architecture of the Jakarta Basin, Indonesia with transdimensional inversion of seismic noise. *Geophysical Journal International*, *204*(2), 918–931.

Saygin, E., Cummins, P. R., & Lumley, D. (2017). Retrieval of the P wave reflectivity response from autocorrelation of seismic noise: Jakarta Basin, Indonesia. *Geophysical Research Letters*, *44*, 792–799. https://doi.org/10.1002/2016GL071363

Sens-Schönfelder, C., Snieder, R., & Stähler, S. C. (2015). The lack of equipartitioning in global body wave coda. *Geophysical Research Letters*, *42*, 7483–7489. https://doi.org/10.1002/2015GL065108

Sun, W., Fu, L.-Y., Saygin, E., & Zhao, L. (2018). Insights into layering in the cratonic lithosphere beneath Western Australia. *Journal of Geophysical Research: Solid Earth*, *123*, 1405–1418. https://doi.org/10.1002/2017JB014904

Sun, W., & Kennett, B. (2016). Receiver structure from teleseisms: Autocorrelation and cross correlation. *Geophysical Research Letters*, *43*, 6234–6242. https://doi.org/10.1002/2016GL069564

Taylor, G., Rost, S., & Houseman, G. (2016). Crustal imaging across the North Anatolian Fault Zone from the autocorrelation of ambient seismic noise. *Geophysical Research Letters*, *43*, 2502–2509. https://doi.org/10.1002/2016GL067715

Tonegawa, T., Nishida, K., Watanabe, T., & Shiomi, K. (2009). Seismic interferometry of teleseismic S-wave coda for retrieval of body waves: An application to the Philippine Sea slab underneath the Japanese Islands. *Geophysical Journal International*, *178*(3), 1574–1586.

Wang, Y., Lin, F.-C., Schmandt, B., & Farrell, J. (2017). Ambient noise tomography across Mount St. Helens using a dense seismic array. *Journal of Geophysical Research: Solid Earth*, *122*, 4492–4508. https://doi.org/10.1002/2016JB013769

Xu, Y., Koper, K. D., & Burlacu, R. (2017). Lakes as a source of short-period (0.5–2 s) microseisms. *Journal of Geophysical Research: Solid Earth*, *122*, 8241–8256. https://doi.org/10.1002/2017JB014808

Zhou, W., & Paulssen, H. (2017). P and S velocity structure in the Groningen gas reservoir from noise interferometry. *Geophysical Research Letters*, *44*, 11,785–11,791. https://doi.org/10.1002/2017GL075592